Journal of The Electrochemical Society, **151** (12) A1989-A1998 (2004)
0013-4651/2004/151(12)/A1989/10/$7.00 © The Electrochemical Society, Inc.

Platinum-Iron Phosphate Electrocatalysts for Oxygen Reduction in PEMFCs

Peter J. Bouwman,[a,b,*] Wojtek Dmowski,[c] Jason Stanley,[a] Gregory B. Cotten,[b] and Karen E. Swider-Lyons[a,*,z]

[a]*Naval Research Laboratory, Surface Chemistry Branch, Washington, DC 20375, USA*
[b]*Department of Chemistry, United States Naval Academy Annapolis, Maryland 21402, USA*
[c]*Department of Materials Science and Engineering, University of Tennessee, Knoxville, Tennessee, USA*

Proton exchange membrane fuel cells (PEMFCs) depend on platinum at the cathode to catalyze the oxygen reduction reaction (ORR) and maintain high performance. This report shows that the electrocatalytic activity of Pt is enhanced when it is dispersed in a matrix of hydrous iron phosphate (FePO). The Pt-FePO has 2 nm micropores with Pt dispersed as ions in Pt^{2+} and Pt^{4+} oxidation states. Increased ORR performance is demonstrated for the Pt-FePO + Vulcan carbon (VC) materials compared to a standard 20 wt % Pt-VC catalyst on rotating disk electrodes with Pt-loadings of 0.1 mg(Pt) cm^{-2}. The improvement in the ORR is attributed to the adsorption/storage of oxygen on the FePO, presumably as iron-hydroperoxides. The ORR activity of the Pt-FePO in air is close to that in oxygen at low current density, and therefore this catalyst has a distinctly unique behavior from Pt-VC. Contrary to Pt-VC, the Pt-FePO catalyst shows activity towards hydrogen and CO oxidation, but does not exhibit their characteristic adsorption peaks, suggesting that Pt ions in the iron phosphate structure are less sensitive to poisoning than metallic Pt. The results present opportunities for new low-Pt catalysts that extend beyond the current capabilities of Pt-VC.
 [DOI: 10.1149/1.1808591]

Manuscript submitted January 30, 2004; revised manuscript received April 5, 2004 Available electronically October 28, 2004.

Proton-exchange membrane fuel cells (PEMFCs) are electrochemical conversion devices that can produce electricity at high fuel efficiencies, and they are currently in development for a wide range of commercial applications. Before the fuel cells become practical for wide-scale consumer use, several technological problems must be solved. For instance, the activity of the electrodes must be improved to increase efficiency, while the amount of platinum (Pt) catalyst in the electrodes must be lowered to reduce the cost of the devices. The issues of activity and Pt loading are greatest at the cathode where the oxygen reduction reaction (ORR) suffers from high overpotentials.[1]

The oxygen reduction reaction (ORR) at a fuel cell cathode is given in Eq. 1 and the hydrogen oxidation reaction (HOR) at the anode is given in Eq. 2

$$\text{ORR } O_2 + 4H^+ + 4e^- \rightarrow 2H_2O \quad [1]$$

$$\text{HOR } H_2 \rightarrow 2H^+ + 2e^- \quad [2]$$

Pt is an ideal catalyst for both these reactions, and the catalytic efficiency per unit weight of Pt is generally improved by decreasing the particle size of the catalysts, as smaller particles exhibit a larger catalytic surface area per unit of volume. However, the success gained by size reduction is limited by three effects. First, the catalytic activity drops with decreasing particle size, because active Pt crystal facets disappear.[2] For example, the fraction of the surface having the most active (100) facets drops rapidly for particles less than 6 nm in diameter and disappears completely at 1.8 nm. Pt particles smaller than 2 nm are formed almost entirely from (111) facets,[3] which exhibit two orders of magnitude lower activity than (100) facets, as shown on single-crystal Pt in sulfuric acid electrolyte.[4] Second, the surface energy increases with the decrease in particle diameter. As a result the reactants are more strongly adsorbed and not easily released. Hence, Pt nanoparticles smaller then 4 nm in diameter show lower activity than expected from their catalytic surface area.[5] The third problem is coagulation or Oswald ripening of Pt nanoparticles over time, which causes a decrease of the active surface area with aging and eventually results in decreased catalyst performance.[6] The ripening of Pt particles can be mediated by alloying with Cr and Co,[7] however stability issues have made many of the alloy compositions impractical.

The Pt loading required on the electrodes has also been decreased by modification of the environment that the catalyst experiences in the membrane electrode assembly (MEA). Researchers at Los Alamos National Laboratory discovered that Pt utilization is improved when the catalyst is dispersed on a porous, electronically conductive substrate (Vulcan carbon, VC) and with a proton-conducting medium (a perfluorosulfonic ionomer, Nafion).[8,9] When surrounded by Vulcan carbon and Nafion, the Pt serves more effectively as an electrocatalyst for the ORR and HOR, because there are ample transport paths for the protons and electrons in Eq. 1 and 2. Whereas the catalytic activity of the Pt is critical, the electrode reactions are mediated by the rate of the transport of the gases, protons, electrons, and water to and from the Pt surfaces. For instance, low protonic conductivity in PEMFC cathodes is understood to be a limit to their performance at high current densities.[10,11] With the Pt activity no longer being the limiting factor, the Pt loading at PEMFC cathodes was reduced by an order of magnitude from 4 mg(Pt) cm^{-2} to 0.4 mg(Pt) cm^{-2}. The Pt loading at the cathode has been decreased to approximately 0.2 mg(Pt) cm^{-2} by further development of all the MEA components.[12] Yet, a further decrease in Pt-loading is needed for the PEM fuel cell to become practical and cost effective.[13]

Our goal is to lower the Pt content of PEMFC cathodes by creating catalysts which exhibit both high catalytic activity and high ionic transport. Hydrous phosphates are an excellent choice of materials for use at fuel cell cathodes, because they can embody a range of desirable properties, including high protonic conduction,[14,15] catalytic activity,[16,17] and thermal stability.[18] Iron orthophosphates are partial oxidation catalysts commonly used for direct conversion of methane into oxygenates and oxidative dehydrogenation.[19-22] The catalytic efficacy of iron phosphate (FePO) is attributed to a redox mechanism between Fe^{+2} and Fe^{+3}.[23] Catalysis is enhanced by the phosphate groups, which act as Brønsted and Lewis acid sites, and the structural water, which stabilize oxy/hydroxyl states of the catalyst or O/OH and PO_4/PO_3OH couples.[24] Good stability and ionic conductivity makes $FePO_4$ suitable for other electrochemical applications. For example, anhydrous, lithiated $FePO_4$ is under intense investigation as the positive electrode for Li-ion batteries.[25] It should be noted that Pt-Fe alloys have already been noted as active ORR catalysts,[26] but Fe-based catalysts are usually avoided in PEM systems as Fe facilitates the degradation of the Nafion membrane.[27,28]

We combine the attractive properties of the hydrous iron phosphates with those of platinum to create a new catalyst material with

* Electrochemical Society Active Member.
z E-mail: Karen.lyons@nrl.navy.mil

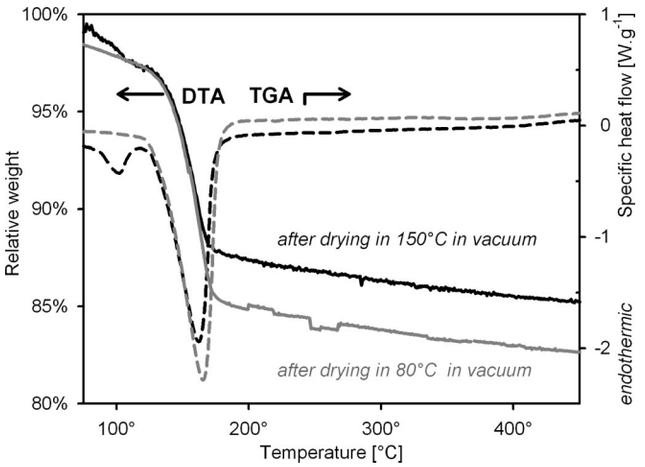

Figure 1. The TGA-DTA data show the Pt-FePO[*i*VC] material contains approximately three structurally bound water molecules per Fe atom, after drying at 80 and 150°C in vacuum.

high ORR activity. Pt is dispersed in hydrous iron phosphate via a sol-gel method, to create a platinum iron phosphate (Pt-FePO). These active materials are characterized for their surface area, microporosity, and the oxidation states of the metals. For electrochemical evaluation, the Pt-FePO is mixed with Nafion ionomer and VC, to eliminate proton and electron transport as possible limiting factors in the electrode performance. The VC and the Pt-FePO are either mixed mechanically (referred to as Pt-FePO + VC), or the VC is impregnated directly with Pt-FePO during synthesis (referred to as Pt-FePO[*i*VC]). The ORR rate of both types of Pt-FePO electrodes are measured using a rotating disk electrode (RDE) half-cell method, so that effects of oxygen-gas diffusion through the electrolyte can be quantified and controlled. The measured ORR current is corrected for these diffusion effects and used to calculate the ORR activity of the catalyst. Finally, the ORR activity of 4.5% Pt-45% hydrous iron phosphate-50% Vulcan carbon is compared to the standard 20 wt % Pt-VC electrode with similar Pt loading, to demonstrate how these unique materials compete with traditional catalyst materials for PEMFCs.

Experimental

Hydrous Pt-iron phosphate (Pt-FePO) was prepared in ambient conditions from aqueous solutions using a method adapted from the literature.[19] Iron nitrate [$Fe(NO_3)_3 \cdot 9H_2O$] and ammonium dihydrogen phosphate ($NH_4H_2PO_4$) were dissolved in 18 MΩ cm water separately in a 1:1 molar ratio, mixed together, and stirred for 1 h. The aqueous mixture of iron and phosphate was doped with 1-10 wt % Pt relative to iron by the addition of $H_2Pt(OH)_6$, and sonicated and stirred overnight to ensure the dissolution of the platinum complex. The pH of the acidic solution was increased to pH 7 by the addition of 1 M ammonium hydroxide, with a gelation process occurring at around pH 3. The gelled precipitate was filtered from the solution, washed with high purity water, dried overnight in air, and then heated in air at 150°C for 12 h. After grinding, the powders were heated again under vacuum for 12 h at 150°C.

The dried Pt-FePO was acid-washed by stirring the powder in 1 M sulfuric acid at 90°C for at least 1 h. The remaining powder was filtered, rinsed with high purity water, and subjected to drying at 150°C again.

The reference material for this study was 19.7 wt % Pt-Vulcan carbon from E-TEK, heretofore referred to as Pt-VC. The material was used as received.

The physical, morphological, and chemical attributes of catalyst materials were ascertained by various methods. The water-content of the Pt-FePO was estimated by simultaneous thermogravimetric analysis and differential thermal analysis (TGA/DTA, Rheometric Scientific) by heating under flow of argon to 500°C at 5°C min^{-1}. The Pt and Fe contents of catalysts were determined by inductively couple plasma measurements (ICP) using a Perkin-Elmer ICP spectrometer (Optima 4300 DVICP-OES). Samples were decomposed in aqua regia by microwave digestion, and the resulting solutions were filtered to remove the carbon and diluted to specific volumes with nitric acid and water. For quality control, field blanks and reagent blanks were prepared and analyzed. Wavelengths for Pt and Fe detection were selected based on detection sensitivity (metal-dependent) and correlation coefficients (>0.9999) of the elements' calibration curves.

The morphology of the catalysts was surveyed by scanning electron microscopy (SEM, Leo 1550) at 2 kV using a Shottky field

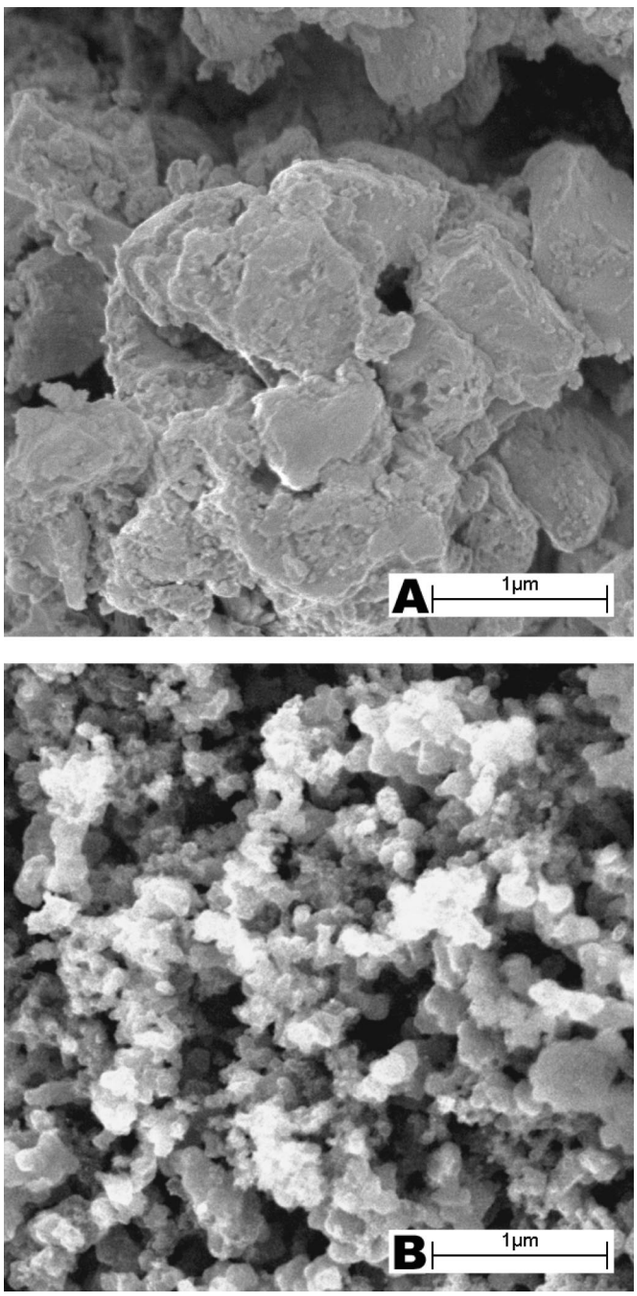

Figure 2. The SEM micrographs show the powder morphology of Pt-FePO (A) and Pt-FePO[*i*VC], (B) after drying in air at 150°C.

Table I. The chemical composition of the acid-washed Pt-FePO[*i*VC] and Pt-FePO catalyst materials as determined by ICP analysis.

	Pt-FePO[*i*VC]		Pt-FePO	
Element	[wt % ± 95%$_{CI}$]	Molar ratio rel. Fe	[wt % ± 95%$_{CI}$]	[10^{-3} mol ± 95%$_{CI}$]
Pt	12.3 ± 1.3 wt %	0.60 ± 0.06%	9.5 ± 1.0%	0.14 ± 0.02%
Fe	5.9 ± 0.6 wt %	1.00 ± 0.10%	18.8 ± 1.9%	1.0 ± 0.10%
P	8.1 ± 0.8 wt %	2.48 ± 0.24%		
O	23.7 wt %	11(+3H_2O) ± 1.6%		
C	50 wt %		0 wt %	

emission gun (Gemini column). Energy dispersive spectroscopy measurements were carried out on the same instrument at 20 kV. The long-range structure of the materials was evaluated by powder X-ray diffraction (XRD; Bruker AXS, D8 Advance, Cu Kα radiation). The surface area and pore size distribution of the powder were determined by the Brunauer-Emmett-Teller (BET) method under N_2/He, and the data were modeled using the Barret-Joyner-Halenda (BJH) adsorption method (Micromeritics ASAP 2010). Prior to the BET measurements, the powders were heated at 150°C under vacuum for 12 h.

The oxidation states of the Pt and Fe were determined both by X-ray photoelectron spectroscopy (XPS, Fisons, monochromatic Al Kα anode) and X-ray absorption near edge spectroscopy (XANES). For analysis in the XPS and electrochemical testing, the powders were mixed with 50 wt % VC and a 0.1% Nafion solution, which was dropped onto a strip of carbon cloth and briefly dried in vacuum at room temperature prior to loading into the instrument. The influence of the electrochemical tests on the oxidation states of the Pt and Fe were studied by first cycling the catalyst/carbon cloth electrode between 0.9 and 0.1 V *vs.* RHE for five cycles at 20 mV s^{-1} under oxygen in 0.1 M $HClO_4$ electrolyte at 60°C. The sample was then removed from the electrochemical cell at open circuit potential (OCP, +0.85 V) and vacuum dried at room temperature before loading in the UHV chamber. The XPS spectra were fitted using the Universal Spectrum Processing program.[29] The backgrounds of the spectra were subtracted prior to the line fits.

The XANES measurements were carried out on the Pt L_3 edge on beamline X-11B at the National Synchrotron Light Source at Brookhaven National Laboratory, using a Si(111) monochromator. Materials were ground with boron nitride and pelletized before mounting in a standard transmission setup with a Pt metal foil as a reference. In addition, fluorescence was measured using Lytle detector placed at a 45° angle to the sample surface. Absorption and fluorescence data were corrected for background and normalized using IFEFFIT software package.[30] Platinum compounds $H_2Pt(OH)_6$, K_2PtCl_4, and $PtCl_2$ were measured as references.

For electrochemical characterization, the Pt-FePO was mixed with Vulcan carbon in two different ways. One method was to physically mix equal weights of VC and the Pt-FePO catalyst powder using a mortar and pestle; this mixture is referred to as Pt-FePO + VC. Alternatively, the VC was impregnated with Pt-FePO by adding the VC during the synthesis stage. In this case, approximately 50 wt % VC was added to the iron nitrate solution described above, before the addition of the ammonium dihydrogen phosphate. The $H_2Pt(OH)_6$ was first dissolved in 85% H_3PO_4 with sonication and heat, and added to the iron nitrate solution, and then the remaining procedures were followed. This impregnated VC material is referred to as Pt-FePO[*i*VC].

The Pt-FePO + VC or Pt-FePO[*i*VC] powders were prepared as inks for analysis on rotating disk electrodes using the method developed by Paulus *et al.*[31] Approximately 10 mg of the catalyst composite was stirred and sonicated in 1 g of a mixture of 26 parts 18 MΩ cm water, 7 parts isopropanol, and 67 parts of a 5 wt % Nafion solution. A small volume (3-6 μL) of the ink was pipetted onto the glassy carbon tip (5 mm in diameter) of a RDE to obtain a loading of 0.02 to 0.1 mg(Pt) cm^{-2}. The ink droplet was dried under a constant, light air flow to create a smooth film that covered the entire surface of the glassy carbon RDE tip. The thickness of the electrode film was calculated from an estimated density to not exceed 10 μm, even when taking into account 50% porosity. Thick film electrodes may suffer from diffusion limitation of the oxygen gas.[32]

Half-cell measurements of the ORR were performed by rotating the catalyst-loaded RDE tip at 400 to 2500 rpm in 30 mL of 0.1 M $HClO_4$ at 60°C. This method has been identified as an accurate means for establishing the ORR with minimal adverse effects from the anion adsorption or gas diffusion.[31] The gas atmosphere in the cell was controlled by bubbling a constant gas flow of 100 mL min^{-1} of argon, air, hydrogen, oxygen, or CO through the electrolyte solution. An EG&G PAR263A potentiostat with CoreWare software was used to cycle the RDE at a scan rate of 5 mV s^{-1} from the OCP of the RDE to 1.00 V and then between 1.00 and 0.05 V *vs.* a hydrogen-impregnated palladium bead (Pd/H) reference electrode. The Pd/H electrode was corrected to a reversible hydrogen electrode (RHE) by measuring the potential at which a Pt‖Pt cell exhibited zero current while cycling in a hydrogen-saturated 0.1 M $HClO_4$ at 60°C (typically about −25 mV *vs.* the Pt/H electrode). The counter electrode in all experiments was a Pt mesh. The current density was calculated using the geometric surface area of the glassy carbon (0.196 cm^2). The ORR activity was extracted from the difference in the current response of the sweeps measured in argon and oxygen to eliminate the contributions of any capacitive currents. The ORR current density was corrected for diffusion limitation to obtain the kinetic current density using the equation[33]

$$I_{kin} = \frac{I_{lim} \cdot I_{ORR}}{I_{lim} - I_{ORR}} \quad [3]$$

where I_{kin} is the kinetic current density, I_{ORR} is the measured ORR current density, and I_{lim} is the limiting current. Here, I_{lim} was the average value of the ORR current density of ten values measured around 0.3 V *vs.* RHE.

Results

Chemical and physical analysis.—The TGA-DTA analysis is shown in Fig. 1 for the Pt-FePO[*i*VC] after heating at 80 and 150°C. A small amount of weight (<2%) is lost below 100°C due to physisorbed water. Between 100 and 200°C, the samples lose between 10 and 13 wt %, presumably due to the loss of chemisorbed (*i.e.*, structural) water. Accordingly, the materials heated to 80 and 150°C both contain approximately 3 H_2O molecules per atom of Fe. Both samples exhibit the same endothermic peak with a maximum at 165°C despite their dissimilar thermal history, which suggests that the 150°C heat-treatment does not affect the chemisorbed water significantly and that the water in the structure can be exchanged reversibly. Note that in the absence of VC, the endotherm peak of Pt-FePO powder is observed at slightly higher temperatures (around 175°C), presumably due to its larger particle size. The weight loss that occurs between 200 to 500°C can be attributed to the gradual removal of protonated surface groups and structural oxygen.

The results from the ICP analysis of the Pt-FePO and Pt-FePO[*i*VC] materials are given in Table I. The Pt concentration of the catalysts is affected both by the amount of Pt added during synthesis and the acid-washing step. For example, Pt-FePO compounds synthesized with 2-5% Pt can have ~10% Pt after the acid washing step; the nonplatinized FePO is removed as an unstable phase. Although the FePO dissolves immediately in 1.0 M phosphoric and sulfuric acid, it is more corrosion resistant with the incorporation of Pt.[d] The remaining acid-washed Pt-FePO[*i*VC] catalyst contains a Pt, Fe, P, and O molar ratio 0.6:1:2.5:14. The calculation of the molar ratios assumes that 50% of the initial sample weight is carbon, and that the balance of unaccounted weight is due to oxygen and a fraction of hydrogen. Also, 3 moles of the oxygen are attributed as chemisorbed H_2O, as determined by the TGA-DTA analysis. The Pt and Fe contents of the Pt-FePO material without VC are also given in Table I.

The morphology of the acid-washed powders Pt-FePO and Pt-FePO[*i*VC] is displayed by the SEM micrographs in Fig. 2A and B, respectively. The dried Pt-FePO comprises agglomerates of nanoparticles with some mesoscale pores. The size of the particle agglomerates is on the order of 1 μm, after grinding with a mortar and pestle. The Pt-FePO[*i*VC] material shows agglomerates of separate particles with diameters of approximately 50 to 100 nm that resemble the particle size and distribution of the VC powder. The impregnated Pt-FePO is distributed homogeneously throughout the VC particles, due to the high porosity of the VC. Scanning EDS measurements confirm a uniform coverage of the Pt, Fe, and P within 2 μm resolution.

The Pt-FePO structure is amorphous to XRD after drying at 150°C as indicated by the XRD pattern shown in Fig. 3. The absence of long-range order suggests that no regular structure exists and that no metallic Pt clusters are formed during the preparation procedure. Specific diffraction peaks are observed when the powder is heated to higher temperatures (800°C for 20 h). When Pt-FePO powder that has not been acid washed is heated to 800°C, it has distinct Pt and $FePO_4$ phases. If the Pt-FePO is acid-washed and then heated to 800°C, there are peaks from Pt crystallites, plus an unidentified phase, presumably an (unidentified) iron phosphate structure.

Structural information has been obtained for the 150°C-heated Pt-FePO powders (before acid washing) via the pair density function (PDF) analysis of high energy X-ray diffraction. This study indicated local order reminiscent of an α-quartz phase.[34] These experiments are being repeated for the acid-washed Pt-FePO. Therefore, although conventional powder XRD indicates an amorphous structure, an ordered local or medium range structure (to 0.5 nm) is likely. The PDF analysis of these materials will be the subject of a forthcoming publication.

The surface area and pore-size distribution are given in Table II for two FePO-based materials that have been heated to 150°C, FePO and acid-washed Pt-FePO. The FePO support structure is microporous and exhibits a surface area of 136 $m^2\ g^{-1}$. This material could not be characterized after acid-washing, because FePO is not stable in acid without Pt. The FePO maintains its high surface area with incorporation of Pt (*i.e.*, 131 $m^2\ g^{-1}$), although the micropores decrease in size from 3.9 to <2 nm. The acid washing procedure has a significant impact on the Pt-FePO structure, as it decreases the BET surface area to 56 $m^2\ g^{-1}$ and introduces a bimodal pore size distribution with both peaks centered around <2 and 11 nm. The BET surface area of the Pt-FePO[*i*VC] compound cannot be measured accurately, due to interference from the VC.

XPS analysis of the Pt-FePO + VC catalyst material before and after electrochemical cycling is compared to that of the standard Pt-VC catalyst. The Pt-FePO + VC before and after cycling has a Fe-$2p_{3/2}$ peak at 712.9 ± 0.7 eV (not shown), which is comparable

[d] In phosphoric acid slow re-precipitation occurs of crystalline $FeH_3(PO_4)_2 \cdot 2H_2O$. Although this pink powder is stable under fuel cell conditions, it is not feasible as a catalyst because it exhibits a low surface area and inferior ORR performance.

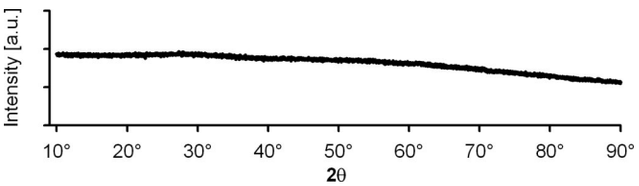

Figure 3. The XRD plot shows that the structure of 9.5 wt % Pt-FePO has no long-range structural order after heat-treatment at 150°C and the acid wash procedure.

to values of 711.4 eV for Fe^{3+} in $FePO_4$ heated to 550°C[35] and 712 to 713.5 eV for Fe^{2+} and Fe^{3+} in phosphate-rich iron glasses.[36] The peak in the Pt-FePO materials is tentatively assigned to Fe^{2+}/Fe^{3+}, as the mixed valence iron state is suggested by structural studies.[35] The Fe-$2p_{3/2}$ signal is unchanged by the electrochemical cycling of the electrode in oxygen, indicating no change in the Fe oxidation states induced by the electrochemical cycle. The O 1s peak is observed near 532.2 eV, but is not considered further due to possible interference from the sulfonic groups in the Nafion ionomer used for electrode preparation.

The raw XPS spectra of Pt in the catalysts are shown in Fig. 4. Pt-VC serves as reference (gray line) and shows a Pt-$4f_{7/2}$ binding energy of 71.3 eV and Pt-$4f_{5/2}$, at 74.6 eV, which is consistent with other reports on carbon-supported Pt-metal clusters.[37] In comparison, the Pt in Pt-FePO + VC bears no resemblance to the Pt-VC both before (dashed black line) and after cycling (solid black line). The Pt-FePO + VC samples have three apparent peaks which can be deconvoluted into two sets of overlapping Pt-$4f_{7/2}$ and Pt-$4f_{5/2}$ doublets, each with the expected 3.3 eV separation. The binding energies of the two Pt-$4f_{7/2}$ peaks are at 73.1 and 76.0 eV in the Pt-FePO. The $4f_{7/2}$ peak at 73.1 eV is attributed to Pt^{2+}. The binding energy is consistent with the values between 72.2 and 73.4 eV reported for the Pt-O and $Pt(OH)_2$ scales that form on Pt metal in nitric acid and under electrochemical treatment.[38,39] The second $4f_{7/2}$ peak at 76.0 eV is attributed to Pt^{4+}, even though the binding energy exceeds 74.4 eV, the reported value for PtO_2.[38,39] These Pt^{4+} species may have a higher binding energy in association with phosphate groups, due to an increase in the bond ionicity, or different atomic environment as occurs for iron phosphate (Fe in Fe_2O_3 has a binding energy of 710.7 eV, while Fe in $FePO_4$ has a binding energy of 711.4 eV[36]). The ratio of Pt^{2+}:Pt^{4+} peak area is approximately 40:60 before cycling and 55:45 after cycling, indicating some reduction of the Pt^{4+} to Pt^{2+}. However, the results clearly show that no Pt metal is present or forms during the electrochemical cycling of the Pt-FePO electrodes. The exact state of the platinum during the ORR reaction is still unknown, because these UHV experiments are inherently *ex situ*. A future experiment is planned for the *in situ* investigation of the oxidation states of these electrodes using X-ray absorption spectroscopy.

Table II. The BET surface area and the average pore size are listed for FePO and the acid-washed 9.5 wt % Pt-FePO.

Catalyst material	BET surface area [$m^2 \cdot g^{-1}$]	Average pore size [nm]
FePO	136 ± 0.3	3.86 ± 0.01
9.5 wt % Pt-FePO (corrected for Pt content)	56.4 ± 0.4(62.3 ± 0.4)	<2 and 11[a]

[a] Bimodal pore size distribution.

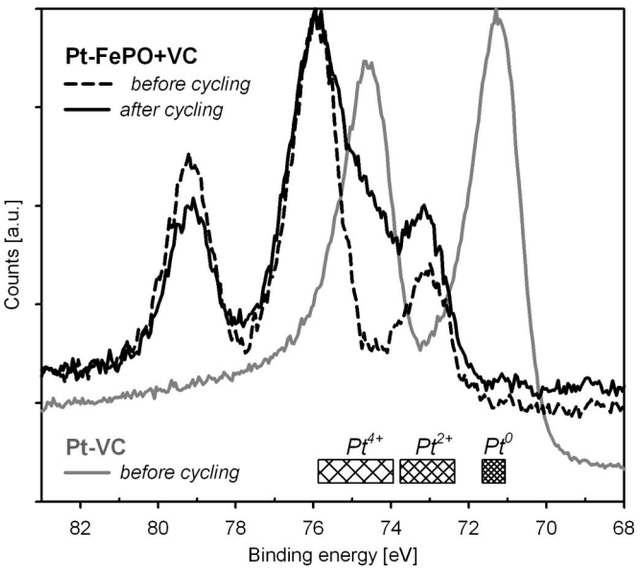

Figure 4. The Pt-4f XPS spectra are shown for Pt-iron phosphate before (dashed black line) and after electrochemical cycling (solid black line) in oxygen and compared to Pt-VC (gray solid line). All spectra are scaled relative to their maximum count. The peak locations indicate that the Pt is metallic on Pt-VC, while it is oxidized in the Pt-FePO + VC. Peak fitting shows a Pt^{2+}:Pt^{4+} ratio of 40:60 in the as-prepared electrode and 55:45 after electrochemical cycling.

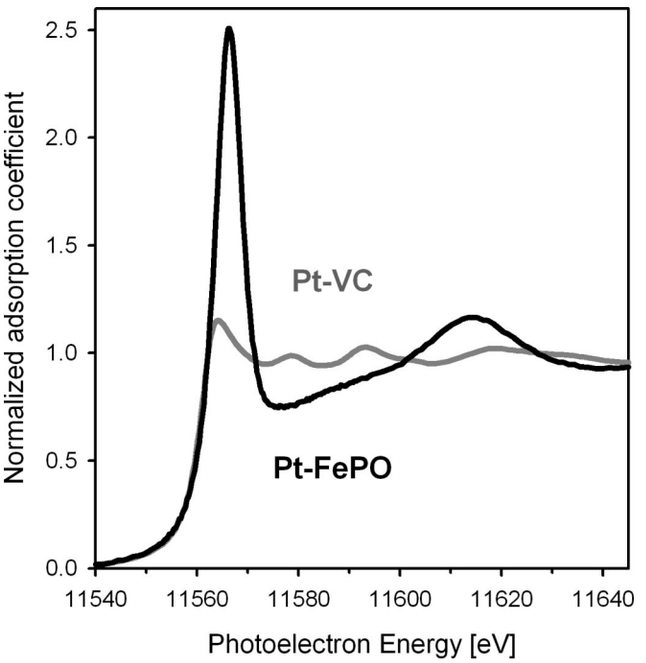

Figure 5. The plot shows the normalized XANES spectra of the acid-washed Pt-FePO catalyst and the Pt-VC standard. The Pt-L_3 absorption edge in Pt-FePO is shifted by ~2.7 eV *vs.* Pt metal foil, which is indicative of an oxide.

Results from the *ex situ* XANES experiment clearly show the ionic character of Pt in the Pt-FePO catalyst. Figure 5 presents the Pt-L_3 edge spectra of the acid-washed Pt-FePO catalyst material (black line) and the Pt-VC standard (gray line). The plotted data and comparison to standards indicate that the Pt in the FePO is oxidized as evidenced by the suppression of the white line in the Pt-FePO.

Electrochemical characterization.—The cyclic voltammetry of FePO + VC (no Pt and not acid-washed) is shown in Fig. 6 under argon (dotted line) and oxygen (solid line) during continuous cycling. During the first cathodic sweep in argon (or oxygen), the FePO + VC electrode has a single large reduction peak at 0.65 V that is designated the activation peak. No remarkable features are observed during further cycling under argon (dotted line). Under oxygen, a reductive current is measured which, as expected for the ORR, increases with the RDE rotation rate, as shown in Fig. 6 for 400 rpm (thin solid line) and 1600 rpm (thick solid line). In each sweep under oxygen, two current regimes can be distinguished with different slopes, the first between 0.9 and 0.3 V and the second between 0.3 and 0.05 V *vs.* RHE. The different reaction rates could indicate different oxygen reduction reaction pathways exist on FePO, but this hypothesis has not been investigated. The FePO support material has insufficient activity to act as a fuel cell catalyst, because the ORR current does not even reach the oxygen diffusion limit.

The activation of the FePO is also observed for Pt-FePO + VC at 0.41 V upon the first cathodic sweep in argon (Fig. 7a). The activation peak is also observed upon the first sweep in oxygen, with the maximum of the activation peak followed directly by the onset of the ORR activity. A corresponding de-activation peak is observed at 1.6 V during extended anodic cycling to 1.7 V (Fig. 7b), and oxygen evolution is observed above 1.8 V. Once the RDE is swept cathodic again to 0.1 V, subsequent reactivation of the Pt-FePO + VC occurs again at 0.4 V *vs.* RHE, although the catalyst has lower ORR activity than before it was deactivated at 1.6 V. If the RDE is only swept between 1.8 and 0.6 V and not reactivated, no ORR activity is observed, but oxygen evolution is measured still above 1.8 V. By comparison with Fig. 5, it is clear that the activation/deactivation process is inherent to the FePO. This process is observed for all FePO-based electrodes at approximately the same potentials, even in the absence of VC. Furthermore, the integrated value of the peak, or the number of electrons involved in the activation (*e.g.*, charge), is equivalent to the moles of Fe in the RDE. The activation process of the FePO is likely due to a transformation of the oxygen species associated with the FePO, as discussed below.

Once the Pt-FePO + VC electrode is activated, significant ORR activity is measured below 1.03 V in oxygen and air. The ORR

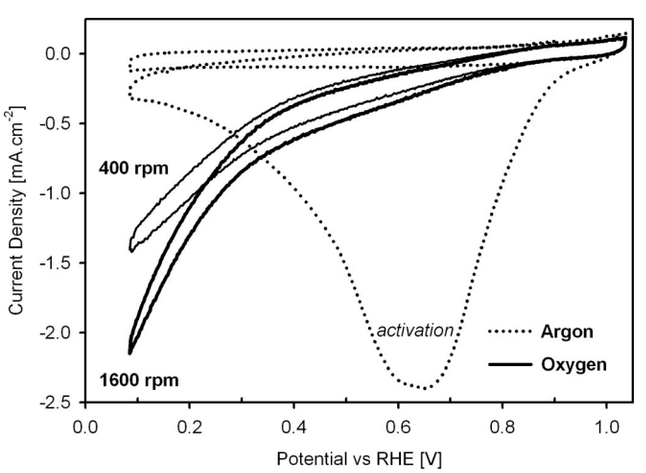

Figure 6. Cyclic voltammograms show the electrochemical activity of the FePO support in the absence of Pt. A typical activation peak is observed only during the first cycle in argon (dotted line). The observed current density in oxygen atmosphere shows minor dependency on the RDE rotation rate and is plotted here for 400 rpm (thin solid line) and 1600 rpm (thick solid line). All CVs are carried out in 30 mL of 0.1 M $HClO_4$ at 60°C with a scan rate of 5 mV s^{-1}.

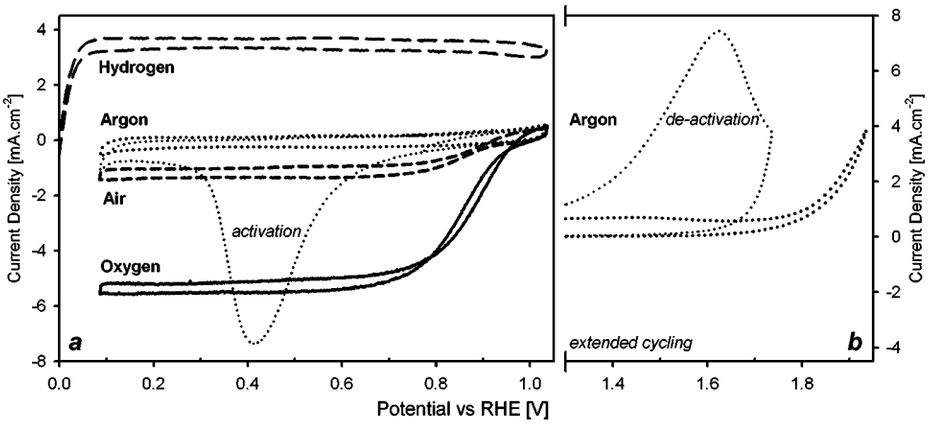

Figure 7. Cyclic voltammograms show the electrochemical behavior of Pt-FePO + VC (0.1 mg(Pt) cm^{-2}) during cycling in argon (dotted line), air (dashed line), hydrogen (long dashed line), and oxygen (solid line). A catalyst activation peak is observed during the first cycle in argon. The corresponding deactivation peak is observed when the cycling range is extended to 1.9 V *vs.* RHE in Fig. 7b (note different current scale).

performance is reproducible for different electrodes and does not degrade with time or cycle number (100 cycles). The RDEs are swept at a low scan rate (5 mV s^{-1}) to minimize the hysteresis caused by the high electrochemical capacitance of the electrode. Faster scan rates shift the cathodic current curve to higher potentials and skew the results to an overestimation of the catalyst performance.

Pt-FePO + VC electrodes also exhibit catalytic activity toward the HOR, as shown by the cycling characteristics of the RDE in hydrogen (Fig. 7a, long dashed line). There is no electrochemical evidence of hydrogen adsorption or desorption peaks on the Pt-FePO + VC, which is distinctly different from the behavior of Pt-VC.[33] The peaks remain absent even when the RDE is cycled at higher scan rates up to 500 mV s^{-1}.[40] The lack of hydrogen adsorption and desorption peaks does not allow the quantification of the effective Pt surface area, as is customary for metallic Pt-based catalysts.[33] We did not evaluate the activity of the catalyst for HOR, due to concerns about the stability of Pt-FePO under hydrogen at low potentials.

The electrochemical behavior of Pt-FePO + VC in a CO atmosphere differs from that of Pt-VC (Fig. 8). The Pt-FePO + VC RDE shows comparable activity for CO oxidation (black solid line), but exhibits a higher ignition potential than observed for metallic Pt on Pt-VC (gray solid line). Also, the typical CO stripping peak located at 0.65 V for the Pt-VC electrode is not detected for the Pt-FePO + VC. Unlike the case with Pt-VC, there is no evidence of any adsorbed CO on the Pt-FePO + VC after the cell has been flushed with argon for 15 min (black dotted line in Fig. 8). Such CO poisoning and subsequent stripping experiments are commonly performed to estimate the effective surface area of catalysts containing Pt metal.[41] However, the CO adsorption characteristics of Pt metal cannot be used for comparison of the electrodes, because this technique provides no information on the active Pt sites in Pt-FePO + VC. These electrochemical results for both hydrogen and CO adsorption are in agreement with the XPS measurements that show no Pt^{o} exists in the phosphate-based catalysts.

The ORR activity of Pt-FePO catalysts is improved further when the Vulcan carbon is impregnated with the catalyst during synthesis. The cyclic voltammetry of a Pt-FePO[*i*VC] RDE is shown in Fig. 9 under argon (dotted line) and under oxygen at different rotation rates (solid lines). The current response in argon is independent of the RDE rotation rate and serves as a reference. Under oxygen, the Pt-FePO[*i*VC] response is similar to that of Pt-VC. The RDE rotation rate has the expected influence on the diffusion-limited current and thus the ORR rate, which is shown by the Levich-Koutechski plot in Fig. 10. In this graph, the inverse of the ORR current densities, taken from the anodic scan at the indicated potentials, are plotted as a function of the inverse of the square of the rotation velocity.

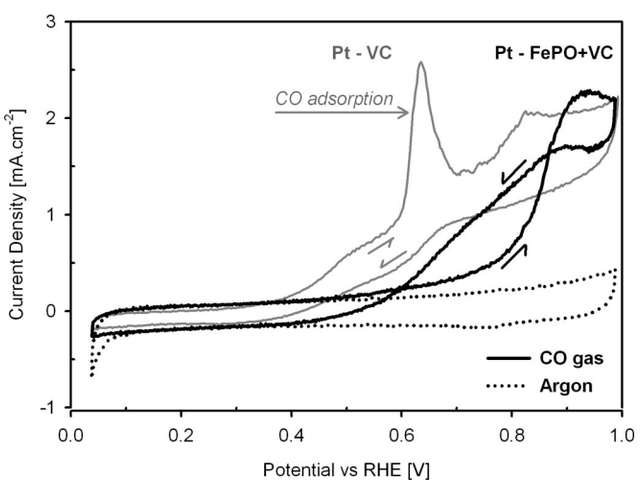

Figure 8. The CO adsorption characteristics of Pt-FePO + VC (thick solid line) are compared to those of Pt-VC (thin solid line) during continuous cycling in CO. In contrast to Pt-VC, the Pt-FePO + VC catalyst does not exhibit a specific CO adsorption peak. No traces of CO could be detected after flushing the cell with argon for 15 min (dotted line).

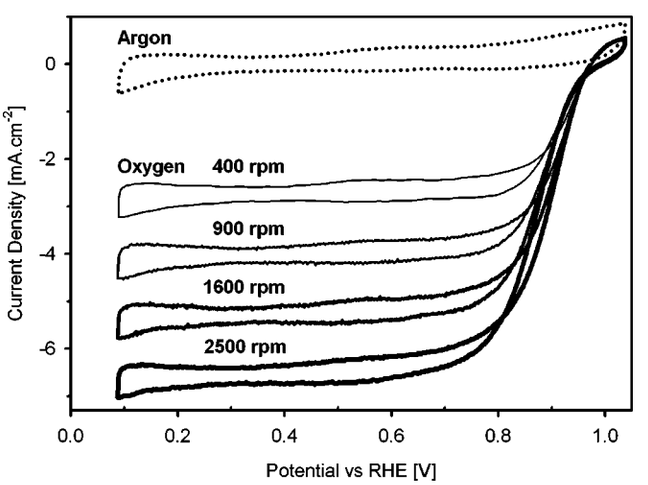

Figure 9. The ORR currents of Pt-FePO[*i*VC] [0.1 mg(Pt) cm^{-2}] are recorded at the RDE rotation rates of 400 to 2500 rpm in oxygen (solid lines). The electrochemical behavior is independent of the RDE rotation rate in argon (dotted line).

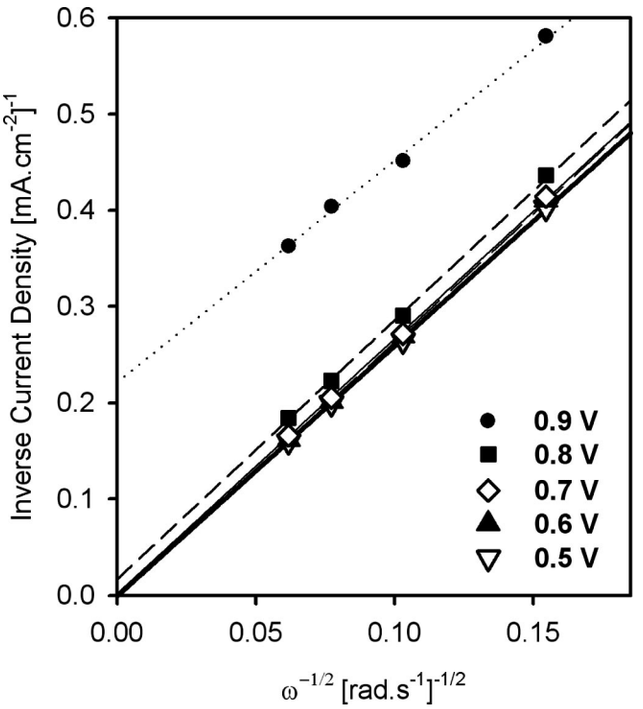

Figure 10. Levich-Koutechski plot derived from the data shown in Fig. 9. The inverse current density is plotted as a function of the inverse square root of the angular RDE velocity for the indicated cell potentials. The data points have been fitted to a linear trend line. Under diffusion-limiting conditions ($\leq$0.7 V) the line intercepts the origin, indicating that the oxygen diffusion resistance of the electrode film is insignificant.

Linear trends can be fitted through the data associated with each half-cell potential, verifying that the ORR is proportional to the supply of oxygen from the electrolyte to the RDE, as predicted from the Levich model.[31,33] The 0.5, 0.6, and 0.7 V lines intercept the origin of the plot, confirming that the internal resistance of the RDEs is insignificant compared to the transport resistance in the electrolyte. Similar Levich-Koutechski plots have been derived for Pt-FePO + VC and Pt-VC RDEs, and these also show linear trends intercepting the origin.

Figure 11 shows a Tafel plot derived from the CVs of the Pt-FePO[*i*VC] (thick solid line) and Pt-VC electrodes (thin solid line) that compares the electrochemical ORR performance of the catalysts at high cell potentials (*e.g.*, low overpotential and minimal oxygen diffusion resistance). The ORR current has been normalized to the Pt-loading of 0.1 mg(Pt) cm^{-2} to obtain the current density per gram of Pt. To compensate for the influence of diffusion at low overpotential, a correction is applied to the measured current densities[e] and the resulting kinetic current densities are plotted in the same graph (dotted lines). The Pt-FePO[*i*VC] exhibits a Tafel slope of -74.2 mV dec^{-1} when fitted to the kinetic current density of the catalysts between 5 and 50 A g^{-1}(Pt), while the Pt-VC shows a slope of -69.8 mV dec^{-1}. The Pt-FePO[*i*VC] catalyst exhibits higher ORR activity than the Pt-VC catalyst at all potentials. The activity is quantified at 0.95 V, and the value for the kinetic current density is listed in Table III, together with the Tafel slopes for the Pt-FePO[*i*VC], Pt-FePO + VC, and Pt-VC electrodes, and shows that the Pt-FePO[*i*VC] exhibits superior ORR activity. For meaningful comparison, all electrodes are prepared identically and have similar limiting current densities (*e.g.*, -5.2 mA cm^{-2} at 1600 rpm and 0.3 V).

[e] The Pt-FePO[*i*VC] electrode contains approximately 12% Pt + 38% FePO + 50% VC and the standard is 20% Pt + VC; we assume that both materials are 50% porous, so the electrodes should be similar in thickness. Note that the thickness of the electrodes has an impact on the values measured and thinner electrodes may appear more active per unit Pt than thicker electrodes due to decreased diffusion resistance.

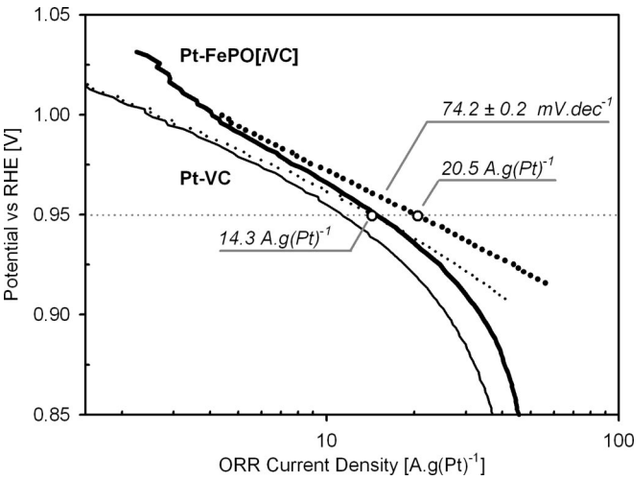

Figure 11. Tafel plot showing the ORR performance of a Pt-FePO[*i*VC] electrode [0.1 mg(Pt) cm^{-2}, thick solid line] *vs.* a Pt-VC electrode is included (thin solid line). The kinetic current density (I_{kin}) has been plotted for both data sets (dotted lines); the values indicate at 0.95 V quantify the catalyst activity and are listed in Table III together with the corresponding Tafel slopes.

The FePO appears to have additional benefits compared to platinum at low current densities and high potentials [>1.0 V and 5 A g^{-1}(Pt)]. In this range, the Tafel slope of the Pt-FePO[*i*VC] electrode shows an unusual increase, suggesting a performance improvement in the margin of ORR activity (Fig. 11). The origin of this reproducible phenomenon is clear from the enlarged CV plots of the Pt-FePO[*i*VC] shown in Fig. 12 for argon (dotted line), air (dashed line), and oxygen (solid line). The half-wave potentials are indicated on the anodic scans as references. Unlike for the Pt-VC, the CVs recorded in argon and oxygen for the Pt-FePO[*i*VC] do not overlap at 1.03 V. Experiments show the baseline of the Pt-FePO catalyst tends to shifts downward in the presence of oxygen. This baseline shift translates to the increased slope in the Tafel plot, as previously indicated. However, the cause of this shift is as yet unexplained. Note that the CV recorded in air overlaps the one measured in oxygen at high potentials, a property also not observed for Pt-VC.[31] Characteristic differences appear in the ORR properties of the Pt-FePO and the Pt-VC catalyst, when their performance at various potentials is studied as a function of the oxygen concentration in the solution.

A new graph, which we refer to as a Tulip plot, is introduced in Fig. 13 to compare the ORR activity of the Pt-FePO catalyst in air *vs.* oxygen. The relative ORR activity in air (*i.e.*, ratio ORR_{air}/ORR_{oxygen}) is plotted as a function of potential for Pt-FePO[*i*VC] (closed triangles) and Pt-VC (open triangles). The ORR current densities in air and oxygen are taken from Tafel plots

Table III. Catalyst activities of three types of electrodes quantified by the kinetic ORR current density measured at 0.95 V *vs.* RHE and listed together with the corresponding Tafel slopes.

Catalyst material	Pt loading [$\mu g(Pt)\cdot cm^{-2}$]	$I_{kinetic}$ at 0.95 V *vs.* RHE [$A\cdot g(Pt)^{-1}$]	Tafel slope [$mV\cdot dec^{-1}$]
Pt-FePO[*i*VC]	98 ± 3	20.5 ± 1.2	74.2 ± 0.2
Pt-FePO + VC	99 ± 4	9.4 ± 0.4	−69.6 ± 0.5
Pt-VC	100 ± 3	14.3 ± 0.7	−69.8 ± 0.8

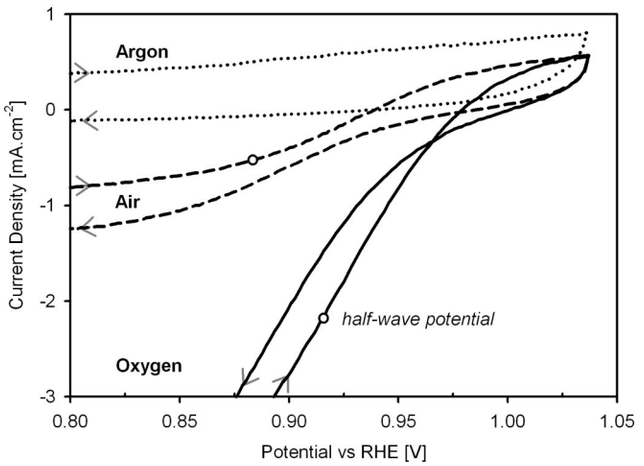

Figure 12. Enlarged cyclic voltammograms showing the onset of the ORR activity of the Pt-FePO[*i*VC] electrode in argon (dotted line), air (dashed line), and oxygen (solid line). The arrows specify the scan direction during cycling and the half-wave potentials are indicated as a reference.

that are not corrected for diffusion. Below 0.85 V, both Pt-FePO[*i*VC] and Pt-VC electrodes experience the same diffusion limitation, when the ORR rate is solely dependent on the oxygen supply through the electrolyte; here, the ORR_{air}/ORR_{oxygen} ratio is equivalent to the oxygen concentration in the electrolyte, or 20%.

The (ORR_{air}/ORR_{oxygen}) ratio increases above 0.85 V (*e.g.*, lower overpotentials) for both catalysts. Apparently, both electrodes experience a higher oxygen concentration at the electrode surface, possibly due to adsorption of oxygen from the electrolyte. Oxygen adsorption is reported on metallic Pt surfaces at >0.85 V.[42,43] For Pt-VC, the ORR ratio decreases from a maximum of 28% at 0.95 V to 0% at 1.01 V. In contrast, the ORR ratio of the Pt-FePO[*i*VC] increases from 36 to 100% between 0.95 and 1.03 V. The enhanced activity of the Pt-FePO electrodes in air suggests that the catalyst maintains its high ORR rate capability under reduced oxygen concentrations at low overpotentials, presumably due to the adsorption of oxygen on the active FePO support material.[40]

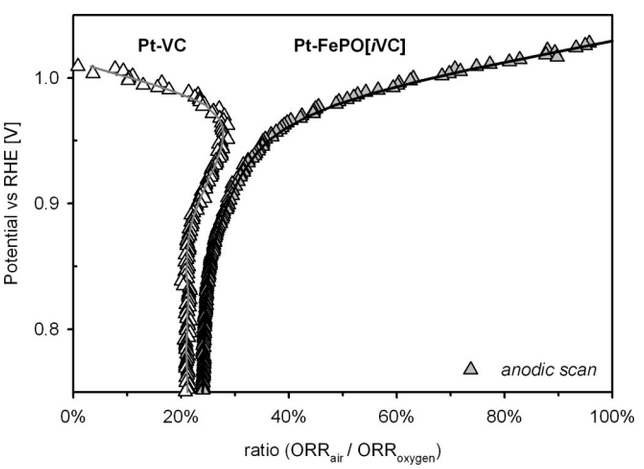

Figure 13. This Tulip plot demonstrates the distinct difference in ORR activity in air *vs.* oxygen between the Pt-FePO[*i*VC] (solid triangles) and Pt-VC electrodes (open triangles) with similar Pt loadings of 0.1 mg(Pt) cm^{-2}. The relative ORR rate in air (normalized to ORR rate in oxygen) is plotted as a function of the potential. Based on the oxygen concentration in air, the expected ORR ratio is around 20% but deviates at low currents where the catalyst and/or adsorption effects become influential.

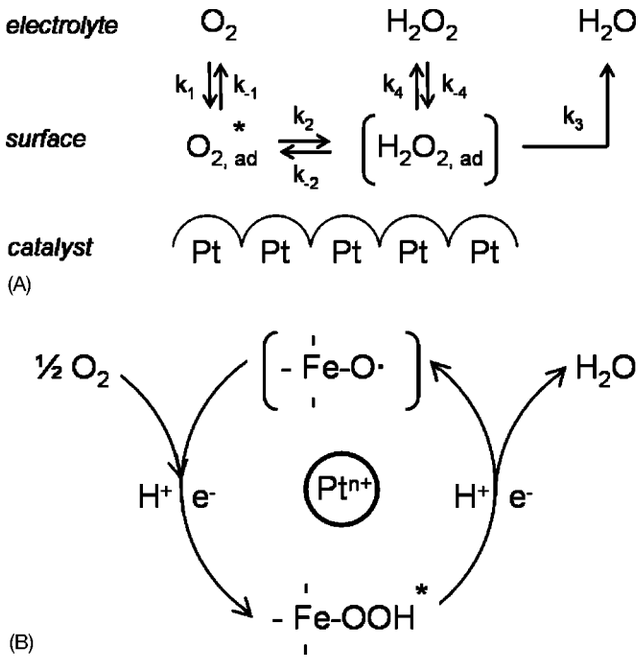

Figure 14. Schematic representation of the basic steps in the ORR mechanism in acid solution on a metallic Pt catalyst (A) and on the Pt-FePO catalyst (B). The stable intermediate hydroperoxide complex is indicated with an asterisk, while the unstable transition state is bracketed.

Discussion

The RDE measurements indicate that the Pt-FePO is unique among state-of-the-art Pt-VC catalysts and is more efficient for the ORR. Despite the ionic Pt^{2+}/Pt^{4+} states in the phosphate catalysts, Pt-FePO[*i*VC] electrodes have increased ORR activity compared to 20 wt % Pt-VC electrodes of similar Pt loading under oxygen. The improvement of the ORR performance of the Pt-FePO appears more pronounced under air at high potentials (*e.g.*, low overpotential), which may be due to the preferential oxygen adsorption on the iron phosphate. Unlike Pt-VC, the Pt-FePO catalysts show no hydrogen and CO gas adsorption characteristics and perhaps are less sensitive to poisoning.

In the Pt-VC catalysts, oxygen reduction occurs on metallic Pt surfaces through dissociative adsorption.[4] A general equation for the ORR mechanism is shown in Fig. 14A. Molecular oxygen is adsorbed to the catalyst surface in the first reaction step k_1. The oxygen is most likely to form a bridged structure on metallic platinum surface, as it binds preferably to two adjacent metal atoms.[44] The O-O bond length of the adsorbed oxygen in the intermediate state, indicated with * in Fig. 14A, is determined by distance between the adsorption sites. Therefore the lattice structure influences the energy barrier associated with transformation to the transition state (step k_2) and sequential reduction of oxygen (step k_3) and thus controls the ORR rate. For example, an alloyed Pt-Fe site exhibits a higher oxygen dissociation rate than a Pt-Pt site, due to a stretched and thus weaker O-O bond.[45] The oxygen dissociation rate on metallic Pt is highest at the step edges of Pt(111) surfaces, where calculations show the enhanced reactivity is caused by increased stabilization of the bridged oxygen and its intermediate adsorption state in the nook between the plane and the rise of the step.[46] Another process that influences the activation energy of the ORR is the significant solvent (*e.g.*, water) reorganization involved with the transition of the intermediate oxygen molecule during its reduction to water.[47] Overall, the oxygen dissociation process (summarized here as step k_2) is considered the rate-limiting step in this ORR mechanism. Once the

O-O is broken, protonation to water is extremely rapid (step k_3) in acid solutions.[48]

The ORR mechanism on the Pt-FePO catalyst is inherently different from the process on Pt-VC as it has no metallic Pt. The Pt^{2+} and Pt^{4+} cations of the Pt-FePO must be surrounded by anions, and they likely exist as platinum hydroxide or peroxide complexes $[Pt(O_xH_y)]$ or as phosphates. The lack of Pt metal and therefore lack of adjacent Pt sites, implies that bridged oxygen adsorption cannot occur on the Pt-FePO. Possibly, the oxygen molecule can bind to a single Pt atom, provided it is not sterically hindered by the coordinating species, but the cycling experiments have shown that the Pt site itself cannot engage oxygen reduction prior to activation of the FePO. This suggests that FePO support is actively involved in the ORR mechanism, presumably through adsorption and/or stabilization of the oxygen on the catalyst.

Iron phosphate is reported to contain active oxygen species that are created through dissociative adsorption of oxygen from the atmosphere or from the bulk lattice to form iron hydroperoxide complexes, or Fe-O-OH.[49] The hydroperoxide complexes are also identified as the catalytically active component in peroxidase enzymes.[50,51] The formation of hydroperoxides is enabled by electrons from the iron redox couple and the surrounding phosphate groups that function as proton donor/acceptor sites (*e.g.*, Lewis acids). Hydroperoxide complexes are stable at room temperature; the breakdown of the peroxides with release of O_2 and return to the initial iron state is sluggish,[52] which is consistent with the observed need for 1.5 V to electrochemical deactivate the iron phosphates (Fig. 7b). Due to their structural stability, the iron hydroperoxide complexes are not chemically aggressive like peroxide in the solution phase (H_2O_2).

The process of iron hydroperoxide formation is the likely origin of the broad reduction or so-called activation peak seen in the first cathodic sweep of the electrode. The (*ex situ*) XPS data indicate that the Pt and Fe do not change oxidation states during the electrochemical activation process. Therefore, it is assumed that the activation mechanism involves a change in the iron coordination from oxygen to peroxide. Apparently, the second oxygen atom in the hydroperoxide group can be drawn from the FePO lattice itself, since the activation process appears uninfluenced by the gas atmosphere. Possibly structural water is converted to hydrogen peroxide, through the addition of a proton and an electron, which then forms the stable iron hydroperoxide complex and activates the ORR capability of the Pt-FePO catalyst. Charge balance may be achieved through the formation or consumption of vacancies.

A basic ORR mechanism is proposed for the activated Pt-FePO catalyst. The schematic representation is shown in Fig. 14B. We hypothesize that oxygen is adsorbed on the iron and, with the reduction of a proton, a hydroperoxide complex is formed in the presence of water. This stable intermediate state can be reduced through proton-assisted heterolysis of the O-O bond to produce water. The remaining Fe-O group needs one electron to compensate its positive charge. However, the now neutral Fe-O$^{\bullet}$ complex is unstable in this environment. In order to achieve full coordination, the oxygen engages another bond with either iron (temporarily creating $Fe^{4+}=O$), with water (reverse reaction) or with another oxygen molecule from the atomsphere. The reaction of Fe-O$^{\bullet}$ with both water and oxygen leads to a stable intermediate state, but only through reduction of oxygen does the catalytic cycle come full circle and produce a net current flow (*i.e.*, the ORR current). In retrospect, the initial activation of the Pt-FePO catalyst is required to create either of these active oxygen complexes and establish this cyclic ORR mechanism.

The role of the Pt in this model would be to boost the dissociation rate of the (stable) intermediate iron peroxide complex. This enhancement would increase the oxygen turnover frequency on the active catalyst sites and thus increase the overall ORR current. Note that according to this ORR mechanism, the presence of neighboring (metallic) Pt sites is not required for the adsorption of oxygen molecules, as is the case for the previously discussed Pt-VC electrodes. Apparently the Pt itself can remain in the oxidized state, while the Pt-site is supplied by the oxygen absorbed on the FePO structure. These data also suggest that other non-Pt ions may be substituted into the FePO to dissociate the peroxide complex. In summary, this ORR mechanism combines the advantage of oxygen storage on the iron phosphate with the high catalytic activity of Pt.

At this point it is not yet clear if the Pt-catalyzed HOR and CO oxidation follow the same mechanism on the Pt-FePO catalyst as on the Pt-VC. Our data suggest that the hydrogen and CO are not adsorbed on the FePO support structure like oxygen. Assuming that hydrogen and CO molecules are directly oxidized on the Pt site without interference from the FePO support, the high HOR rate suggests that the Pt site remains readily accessible to gasses from the electrolyte solution, despite its oxidized state. The high Pt accessibility also implies a large effective Pt surface area and appears to contradict the absence of typical hydrogen or CO adsorption characteristics. For instance, the Pt-FePO + VC electrode shows strong HOR activity during rapid cycling in hydrogen, but does not show evidence of hydrogen peaks even at scan rates up to 500 mV s^{-1}. It can be argued that hydrogen and CO species do not adsorb as strongly on oxidized Pt as they would on a metallic Pt surface, but the activated FePO support could assist in the rapid oxidation of these chemisorbed species on the Pt site through its available supply of stored oxygen. For example, increased CO oxidation activity is observed on a metallic Pt-alumina catalyst promoted with iron oxide, as this iron oxide provides oxygen to the CO adsorbed on the Pt.[53] If the rate of adsorption and subsequent oxidation is increased beyond the timescale of the measurement, the active catalyst sites on the Pt-FePO will appear unoccupied and the typical hydrogen and CO adsorption/desorption peaks are not observed. Whether the chemisorption of hydrogen or CO occurs quickly or not at all, the active Pt sites are not continuously blocked by reactant species. The site availability provided by the nature of the Pt-FePO catalyst could benefit the Pt efficiency and prevent poisoning.

The ORR activity of the Pt-FePO catalyst may be improved further by materials engineering. Targets for optimization are the catalyst particle size and the intrinsic material properties. Reducing the particle size of the catalysts will increase the surface area and benefit the electronic conductivity of the electrode, as each particle will have more contact with the carbon phase. Doping the Pt-FePO with other cations could increase catalytic activity[49] and may benefit its long-term chemical stability as well. Preliminary experiments have shown the fuel cell feasibility of a symmetrical Pt-FePO MEA operating on hydrogen and oxygen, although long-term exposure to hydrogen does lead to catalyst reduction and appearance of metallic Pt. We are also exploring alternative catalyst support materials, which also have high stability and the capability to store oxygen, such as hydrous SnO_x, $TaPO_x$ and $NbPO_x$,[34] that do not have the possible deleterious effects of trace iron on a Nafion membrane.

Conclusions

The efficiency of Pt as ORR catalyst is enhanced by its incorporation into an amorphous hydrous iron phosphate. The ORR activity of Pt-FePO[*i*VC] electrodes at 0.95 V is 20.5 A $g(Pt)^{-1}$, compared to 14.3 A $g(Pt)^{-1}$ measured for a Pt-VC electrodes with a loading of 0.1 mg(Pt) cm^{-2}. The improved performance of Pt-FePO catalysts is attributed to an alternative ORR mechanism that actively involves the FePO support structure. The oxygen is first adsorbed in the form of iron-hydroperoxide complexes, which are then rapidly reduced to water in the presence of Pt. The oxygen storage capability of the FePO benefits the ORR activity particularly at low oxygen concentrations in air. No metallic Pt is present on the ORR-active Pt-FePO catalyst. No hydrogen or CO adsorption characteristics could be detected, which suggests the ionic form of Pt on the Pt-FePO catalyst exhibits lower sensitivity to poisoning than metallic Pt-based catalysts. Although the practical and long-term use of the Pt-FePO materials in PEMFCs must still be proven, these active catalysts

may point to new research directions for low-Pt ORR electrodes, away from the current stalemate in the application of Pt-VC electrodes.

Acknowledgments

The authors are grateful for financial support provided by the Department of Energy Office of Transportation Technologies (contract DE-A101-00EE50639) and the Office of Naval Research. Dr. Shyam Kocha and Dr. Hubert Gasteiger of General Motors Fuel Cell Activities generously provided invaluable scientific discussions and guidance on the RDE experiments. Collaboration with Dr. Francisco Uribe (Los Alamos National Laboratory) contributed to the successful preparation of catalyst inks. We thank Norma Ugarte of the University of Texas—El Paso for the ICP analysis. The operation of the National Synchrotron Light Source is supported by the Department of Energy Divisions of Materials and Chemical Sciences.

The Naval Research Laboratory assisted in meeting the publication costs of this article.

References

1. D. M. Bernardi and M. W. Verbrugge, *J. Electrochem. Soc.*, **139**, 2477 (1992).
2. M. L. Sattler and P. N. Ross, *Ultramicroscopy*, **20**, 21 (1986).
3. K. Kinoshita, *Electrochemical Oxygen Technology*, John Wiley & Sons, New York (1992).
4. N. M. Marković, T. J. Schmidt, V. Stamenković, and P. N. Ross, *Fuel Cells*, **1**, 105 (2001).
5. M. Peukert, T. Yoneda, R. A. Dalla Betta, and M. Boudart, *J. Electrochem. Soc.*, **13**, 309 (1988).
6. M. S. Wilson, F. H. Garzon, K. E. Sickafus, and S. Gottesfeld, *J. Electrochem. Soc.*, **140**, 2872 (1993).
7. P. Stonehart, *J. Appl. Electrochem.*, **22**, 995 (1992).
8. I. D. Raistrick, U.S. Pat. 4,876,115 (1989).
9. M. S. Wilson, J. A. Valerio, and S. Gottesfeld, *Electrochim. Acta*, **40**, 355 (1995).
10. F. Jouen, G. Lindbergh, and G. Sundholm, *J. Electrochem. Soc.*, **149**, A437 (2002).
11. M. Eikerling and A. A. Kornyshev, *J. Electroanal. Chem.*, **453**, 89 (1998).
12. S. Gamburzev and A. J. Appleby, *J. Power Sources*, **107**, 5 (2002).
13. *Multi-Year Research, Development and Demonstration Plan, Planned Activities for 2003-2010, Hydrogen, Fuel Cells & Infrastructure Technology Program*, U.S. Department of Energy, Division of Energy Efficiency and Renewable Energy (2003).
14. K. D. Kreuer, *Chem. Mater.*, **8**, 610 (1996).
15. P. Colomban and A. Novak, in *Proton Conductors: Solid, Membranes and Gels—Materials and Devices*, p. 38, P. Colomban, Editor, Cambridge University Press, Cambridge (1992).
16. R. A. W. Johnstone, J. Y. Liu, L. Lu, and D. Whittaker, *J. Mol. Catal. A: Chem.*, **191**, 289 (2003).
17. J. B. Moffat, *Catal. Rev. - Sci. Eng.*, **18**, 199 (1978).
18. G. Alberti and M. Casciola, *Solid State Ionics*, **97**, 177 (1997).
19. M. Ai and K. Ohdan, *J. Mol. Catal. A: Chem.*, **159**, 19 (2000).
20. M. M. Gadgil and S. K. Kulshreshtha, *J. Solid State Chem.*, **111**, 357 (1994).
21. K. Otsuka and Y. Wang, *Appl. Catal. A*, **222**, 145 (2001).
22. J. M. M. Millet, *Catal. Rev. - Sci. Eng.*, **40**, 38 (1998).
23. J. M. Campelo, M. S. Climent, J. M. Marinas, A. A. Romero, J. A. Navio, and M. Macias, *J. Mater. Chem.*, **5**, 2019 (1995).
24. J. C. Védrine, *Top. Catal.*, **11/12**, 147 (2000).
25. A. K. Padhi, K. S. Nanjundaswamy, and J. B. Goodenough, *J. Electrochem. Soc.*, **144**, 1188 (1997).
26. T. Toda, H. Igarashi, and M. Watanabe, *J. Electroanal. Chem.*, **460**, 258 (1999).
27. A. Pozio, R. F. Silva, M. De Francesco, and L. Giorgi, *Electrochim. Acta*, **48**, 1543 (2003).
28. A. B. LaConti, M. Hamdan, and R. C. McDonald, in *Handbook of Fuel Cells—Fundamentals Technology and Applications*, Vol. 2, W. Vielstich, H. Gasteiger, and A. Lamm, Editors, John Wiley & Sons, London (2003).
29. R. Hesse, Universal Spectrum Processing Program for Esca-Spectra, ver. 32-34, University of Leipzig (2001).
30. B. Ravel, EXAFS analysis software, http://feff.phys.washington.edu/~ravel/ (2003).
31. U. A. Paulus, T. J. Schmidt, H. A. Gasteiger, and R. J. Behm, *J. Electroanal. Chem.*, **495**, 134 (2001).
32. J. A. Bard and L. R. Faulkner, *Electrochemical Methods*, p. 283, John Wiley & Sons, New York (1980).
33. S. L. Gojković, S. K. Zecević, and R. F. Savinell, *J. Electrochem. Soc.*, **145**, 3713 (1998).
34. K. Swider Lyons, P. J. Bouwman, N. Ugarte, and W. Dmowski, *2003 Annual Progress Report, Hydrogen, Fuel Cells, and Infrastructure Technologies*, p. IV-231, U.S. Department of Energy Efficiency and Renewable Energy (2003).
35. X. Wang, Y. Wang, Q. Tan, Q. Guo, Q. Zhang, and H. Wan, *J. Catal.*, **217**, 457 (2003).
36. R. K. Brow, C. M. Arens, X. Yu, and E. Day, *Phys. Chem. Glasses*, **35**, 132 (1994).
37. J. B. Goodenough, A. Hamnett, B. J. Kennedy, R. Manoharan, and S. A. Weeks, *Electrochim. Acta*, **35**, 199 (1990).
38. K. S. Kim, N. Winograd, and R. E. Davis, *J. Am. Chem. Soc.*, **93**, 6296 (1971).
39. J. S. Hammond and N. Winograd, *J. Electroanal. Chem.*, **78**, 55 (1977).
40. P. J. Bouwman, W. Dmowski, and K. E. Swider-Lyons, in *Advanced Materials for Fuel Cells and Batteries*, G. Ehrlich, Editor, PV 2003, The Electrochemical Society Proceedings Series, Pennington, NJ (2004).
41. Y. Morimoto and E. B. Yeager, *J. Electroanal. Chem.*, **441**, 77 (1998).
42. N. M. Marković, T. J. Schmidt, B. N. Grgur, H. A. Gasteiger, R. J. Behm, and P. N. Ross, *J. Phys. Chem. B*, **103**, 8568 (1999).
43. P. G. Allen, S. D. Conradson, M. S. Wilson, S. Gottesfeld, I. A. Raistrick, J. Valerio, and M. Lovato, *J. Electroanal. Chem.*, **384**, 99 (1995).
44. B. C. Stipe, M. A. Rezaei, and W. Ho, *J. Chem. Phys.*, **107**, 6443 (1997).
45. Z. D. Wei, F. Yin, L. L. Li, X. W. Wei, and X. A. Liu, *J. Electroanal. Chem.*, **541**, 185 (2003).
46. P. Gambardella, Z. Sljivancanin, B. Hammer, M. Blanc, K. Kuhnke, and K. Kern, *Phys. Rev. Lett.*, **87**, 056103 (2001).
47. C. Hartnig and M. T. M. Koper, *J. Electroanal. Chem.*, **532**, 165 (2002).
48. N. M. Marković and P. N. Ross, *Surf. Sci. Rep.*, **45**, 121 (2002).
49. K. Otsuka and Y. Wang, *Appl. Catal. A*, **222**, 145 (2001).
50. G. Roelfes, M. Lubben, R. Hage, L. Que, and B. L. Feringa, *Chem.-A Eur. J.*, **6**, 2152 (2000).
51. D. L. Harris and G. H. Loew, *J. Am. Chem. Soc.*, **120**, 8941 (1998).
52. Z. Sun and A. C. C. Tseung, *Electrochem. Solid-State Lett.*, **3**, 413 (2000).
53. X. Liu, O. Korotkikh, and R. Farrauto, *Appl. Catal. A.*, **226**, 293 (2002).